In Situ Polymerized Polyaniline Coating on $Na_5V_{12}O_{32}$ Nanobelts for Enhanced Cycling Stability in Aqueous Zinc-Ion Batteries

Shanjie Wang, Qiang Wen, Xiangbo Huang, Guoqi Qiao, Xin Yu, Xiaohui Tang,* Shaohui Li,* and Jingwei Chen*

Vanadium-based compound cathodes have received considerable attention for aqueous zinc-ion batteries (AZIBs) owing to their high specific capacity, multiple valence states, and versatile structural features. However, the dissolution and severe structural degradation of vanadium-based cathodes during repeated insertion/extraction of Zn^{2+} result in rapid capacity decay, hindering their development. To address these challenges, polyaniline (PANI)-coated $Na_5V_{12}O_{32}$ nanobelt cathodes (NVOP-3) are developed via hydrothermal synthesis combined with in situ polymerization. The in situ-grown PANI coating constructs a dual-functional interface that stabilizes the vanadium oxide framework, prevents its dissolution, and enhances zinc-ion diffusion kinetics. When applied as a cathode for AZIB, the obtained compound delivered a high reversible capacity of 301.5 mAh g^{-1} at 0.1 A g^{-1}, along with remarkable cycling stability-retaining 92.5% of its capacity after 1000 cycles at 2 A g^{-1}, surpassing most reported vanadium-based cathodes. This interfacial engineering strategy offers novel insights for developing robust AZIB cathodes toward practical applications.

1. Introduction

With the rapid development of intermittent renewable energy sources (e.g., solar and wind energy), grid-scale energy storage systems have drawn mounting attention in recent years.[1–4] Lithium-ion batteries hold a dominant position in the consumer electronics industry, courtesy of their high energy density and well-established technological frameworks. However, inherent drawbacks like lithium scarcity and high manufacturing costs limit their suitability for grid-scale energy storage applications.[5,6] Potassium/sodium-ion batteries (KIBs/NIBs), developed in recent years, have shown potential as alternatives owing to their use of abundant alkali metal elements. Nevertheless, issues such as potential safety hazards of electrolytes (e.g., flammability) and insufficient cycle stability of anode materials in existing systems remain unsolved, which seriously limit their application in grid-scale scenarios.[7–11]

Aqueous metal-ion batteries (AMIBs) have demonstrated significant application prospects in grid-scale energy storage, thanks to their intrinsic safety, environmental compatibility, and low cost.[12,13] Among them, aqueous zinc-ion batteries (AZIBs) are specifically recognized as a strategic development direction for next-generation energy storage technologies, owing to their distinctive advantages: a high theoretical capacity (820 mAh g^{-1}/5855 mAh cm^{-3}), good reversibility in aqueous electrolytes, and low redox potential (-0.763 V vs. SHE).[14,15] Over the past few years, various cathode materials, including vanadium- and manganese-based compounds, Prussian blue analogs, and organic compounds, have been widely investigated.[16,17] Among these candidates, vanadium-based cathodes have gradually emerged as a research focus in this field, attributed to their high theoretical specific capacity (>300 mAh g^{-1}), adjustable crystal configurations, and abundant vanadium ore resources.[18,19] Layered vanadium oxides (e.g., V_2O_5, VO_2) can provide fast ion transport channels for Zn^{2+} insertion/extraction due to their open layered structures. For instance, V_2O_5, which forms a 4.37 Å interlayer spacing via $[VO_5]$ trigonal bipyramids, exhibits a theoretical capacity of 589 mAh g^{-1}.[20,21] Nevertheless, the intrinsic poor electronic conductivity of these materials, coupled with structural collapse during charge/discharge cycles, results in actual rate capability and cycle stability that are far below theoretical expectations, severely hindering their engineering application.[22–25]

S. Wang, G. Qiao, X. Yu, S. Li
School of Materials Science and Engineering
Zhengzhou University
Zhengzhou 450001, P. R. China
E-mail: shaohuili@zzu.edu.cn

Q. Wen, X. Huang
Fujiang Energy Technology Co. Ltd.
Hangzhou 311508, P. R. China

X. Tang
Institute of Medical Chips
Shanghai Jiao Tong University School of Medicine
Ruijin Hospital
Shanghai 200025, P. R. China
E-mail: xiaohui.tang@shsmu.edu.cn

J. Chen
Qingdao Key Laboratory of Marine Extreme Environment Materials
School of Materials Science and Engineering
Ocean University of China
Qingdao 266404, P. R. China
E-mail: chenjingwei@ouc.edu.cn

Batteries & Supercaps

Research Article
doi.org/10.1002/batt.202500583

Chemistry Europe
European Chemical
Societies Publishing

To address these problems, introducing cation stabilizers (e.g., Na^+, K^+, NH_4^+, and Zn^{2+}) is considered a simple and effective approach.[26] The incorporation of these cations can expand the layer spacing, promote Zn^{2+} transfer, modify the electronic structure to improve conductivity, and create vacant sites, thereby enhancing electrochemical performance.[27–29] For instance, Mai et al. successfully prepared $Na_{0.33}V_2O_5$ (NVO), which exhibits a high capacity (367.1 mAh g^{-1} at 0.1 A g^{-1}) and outstanding cycle stability (over 93% of its capacity is maintained after 1000 cycles).[30] However, the mere introduction of stabilizing cations cannot resolve the dissolution of vanadium-based materials in aqueous electrolytes or the structural degradation caused by ion insertion/extraction.[19] Conductive polymer surface modification (e.g., polyaniline, PANI) has emerged as an effective strategy to boost both structural stability and ionic conductivity in vanadium-based cathodes. For instance, Sun et al. successfully developed a hybrid material by wrapping $V_2O_5 \cdot nH_2O$ nanobelts with PANI (VOH@PANI). The resulting core–shell cathode maintained 98% capacity after 2000 cycles (2 A g^{-1}), while PANI's ionic conductivity improvement and capacity contribution enabled a high specific capacity of 440 mAh g^{-1} at 0.1 A g^{-1}.[31] Thus, integrating cation intercalation with conductive polymer surface coating could yield a high-performance cathode with both remarkable rate capability and long-term lifespan.

In this work, we synthesized polyaniline (PANI)-wrapped $Na_5V_{12}O_{32}$ (NVO) nanobelts (denoted as NVOP-3) via a hydrothermal method combined with in situ polymerization. The PANI layer in situ grown on the NVO surface enhances ion/electron conductivity, inhibits vanadium dissolution and structural collapse, thereby contributing to high specific capacity and remarkable long-term lifespan. Specifically, NVOP-3 exhibits a high reversible capacity of 301.5 mAh g^{-1} at 0.1 A g^{-1} and exceptional cycling stability, maintaining 92.5% of its capacity after 1000 cycles. Our findings offer critical strategies to address vanadium oxide dissolution and improve their structural stability, while also providing a reference for the research and application of vanadium-based cathodes in AZIBs.

2. Results and Discussion

The two-step synthesis process for NVOP is depicted in **Figure 1**a. First, nanobelt-shaped NVO was synthesized via a simple hydrothermal reaction. Subsequently, NVO served as an oxidative template to trigger the in situ interfacial polymerization of aniline
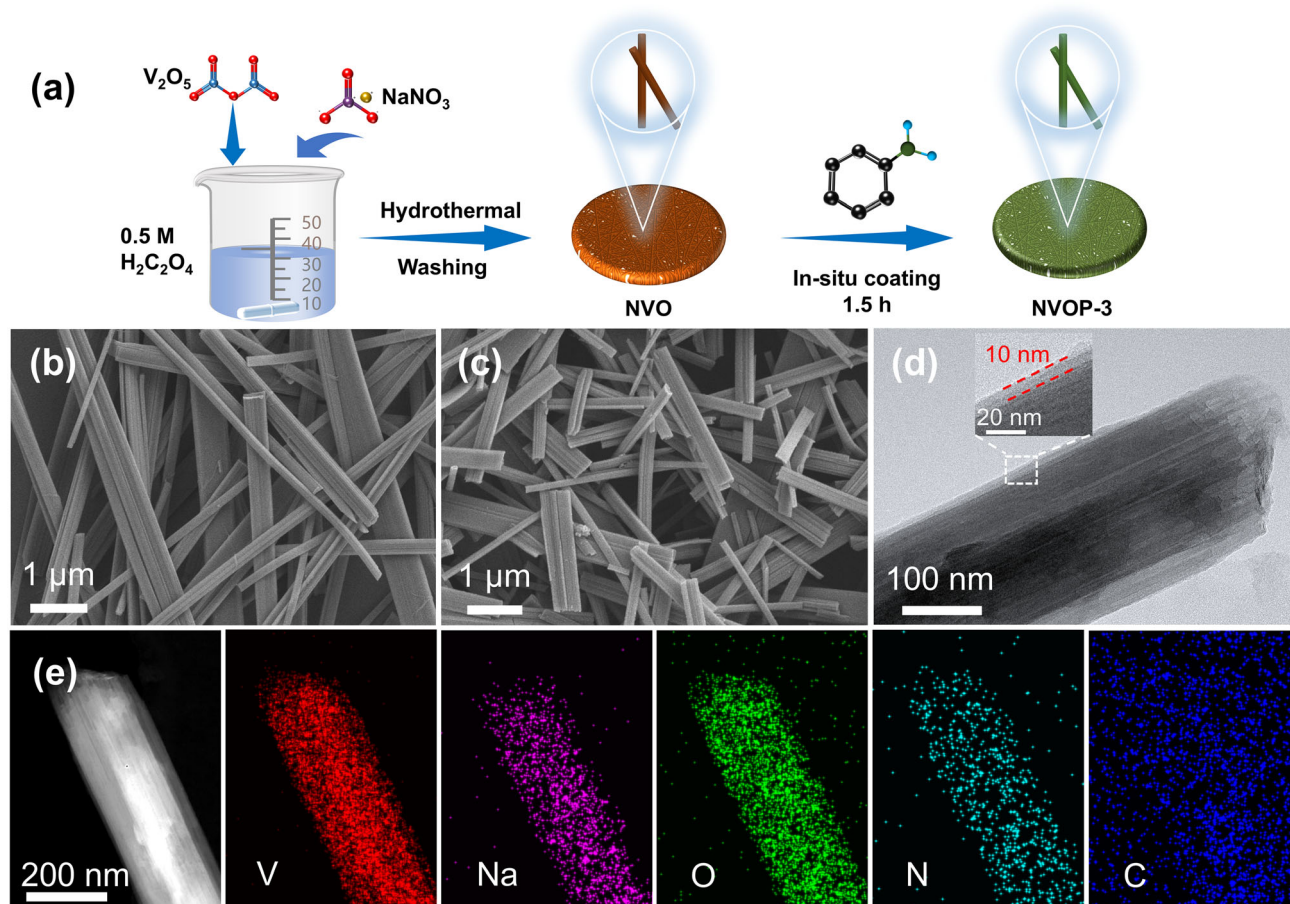

Figure 1. a) Schematic illustration of the synthesis process for NVOP-3. SEM images of b) NVO and c) NVOP-3. d) TEM image of the NVOP-3. e) TEM-EDS element mappings of NVOP-3.

Batteries & Supercaps

Research Article
doi.org/10.1002/batt.202500583

Chemistry Europe
European Chemical
Societies Publishing

monomers, leading to the formation of a conductive PANI coating layer on the outer surface of the nanobelts. Additionally, a diluted H_2SO_4 solution was introduced during the in situ coating process; this not only provided an optimal reaction environment for the in situ oxidation of aniline monomers, but also enhanced the ionic conductivity of the PANI coating layer to a certain extent through proton doping.[32] The core–shell structure of NVOP is expected to reinforce the structural integrity of NVO and suppress vanadium dissolution.

Figure 1b and Figure S1, Supporting Information show the scanning electron microscopy (SEM) morphologies of NVO, revealing that the NVO material consists of nanobelts with widths ranging from 50 to 500 nm and lengths of 10–50 μm. After PANI coating (Figure 1c and Figure S2, Supporting Information), the typical nanobelt structure of NVO is well retained, with no agglomeration of organic PANI observed, indicating that the PANI coating layer grows uniformly on the surface of NVO nanobelts. Additionally, due to their high aspect ratio, NVO nanobelts make a significant contribution to the ion and electron transport kinetics of the material, rendering them suitable as cathode materials for AZIBs.[33,34] The transmission electron microscopy (TEM) image (Figure 1d) reveals that the PANI layer is uniformly coated on the outer surface of NVO, with a distinct boundary between the NVO and PANI layers clearly visible in the insert of Figure 1d and Figure S3, Supporting Information. The PANI coating has a thickness of ≈10 nm. As depicted in the TEM-EDS mapping (Figure 1e), the uniform distribution of V, Na, O, N, and C elements confirms the homogeneous coating of PANI on the surface of NVO nanobelts. The incorporation of Na stabilizers and the

PANI coating can enhance the mechanical strength and structural integrity of NVO nanobelts, further enhancing their rate capability and long-term lifespan. To calculate the amount of PANI in the NVOP-3 sample, thermogravimetric analysis was performed in air. As shown in Figure S4, Supporting Information, the weight loss observed below 100 °C is attributed to the desorption of physically adsorbed water. Meanwhile, the weight loss occurring between 100–500 °C is ascribed to the thermal decomposition of PANI. Based on these weight loss data, the content of PANI in the NVOP-3 is calculated to be 7.6%.

To analyze the phase structure of the as-prepared samples, X-ray diffraction (XRD) was employed, and the result is presented in **Figure 2**a. All sharp diffraction peaks of NVO and NVOP are well matched with the highly crystalline $Na_5V_{12}O_{32}$ phase (JCPDS No.24−1156), with no other impurity peaks observed, manifesting a high level of crystalline phase purity. Specifically, prominent peaks located at 22.96, 27.68, and 50.46° correspond to the (300), (102), and (002) crystal planes of $Na_5V_{12}O_{32}$, respectively. Significantly, the peak intensity of NVOP is slightly weaker than that of NVO, which is attributed to an increase in the amorphous fraction. The phenomenon may result from either the masking of the crystalline signal by the PANI coating or the presence of oxygen vacancies, both of which weaken the characteristic features of the crystal structure.

Fourier transform infrared (FTIR) spectroscopy and Raman spectroscopy were employed to analyze the molecular structure and functional groups of the samples. The FTIR spectra of the as-prepared NVO and NVOP-3 materials are presented in Figure 2b. Key vibrational bands are identified as follows: the peak at
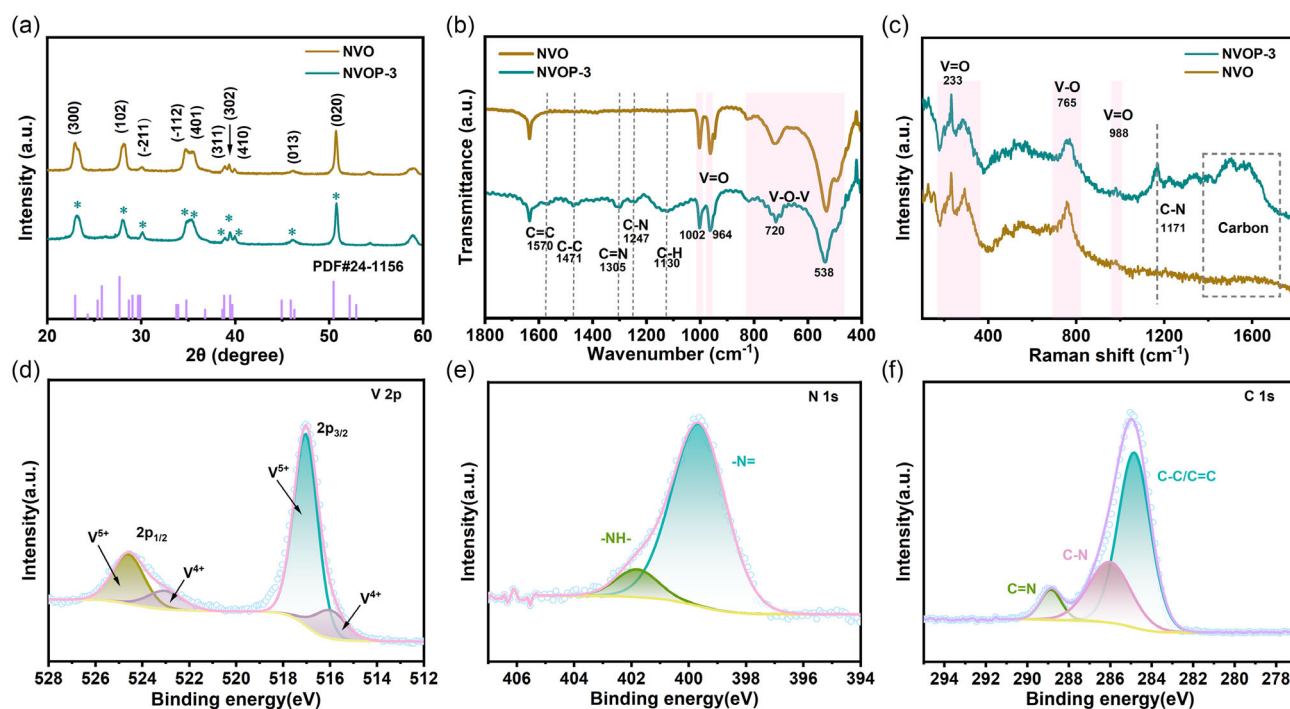

Figure 2. a) XRD patterns, b) FTIR spectra, and c) raman spectra of NVO and NVOP-3. d) V 2p XPS spectrum, e) N 1s XPS spectrum, and f) C 1s XPS spectrum of NVOP-3.

Batteries & Supercaps

Research Article
doi.org/10.1002/batt.202500583

**Chemistry
Europe**

European Chemical
Societies Publishing

1633 cm^{-1} corresponds to the O–H bending vibration of crystalline water,[35] while the peak located at 1002 cm^{-1} is assigned to the asymmetric stretching vibration of the V=O bond.[36] Peaks observed within the 400–800 cm^{-1} region are collectively assigned to the symmetric stretching mode of the V—O—V bond.[37] Compared with NVO, additional characteristic peaks of PANI were observed in NVOP-3: the peaks near 1130, 1471, and 1530 cm^{-1} correspond to the C–H, C–C, and C=C stretching vibrations of the benzene ring, respectively, while the peaks at 1247 and 1305 cm^{-1} are assigned to C–N and C=N stretching vibrations.[38,39] Similar structural information is also observed in the Raman spectrum (Figure 2c). The bands at 233 cm^{-1} and 988 cm^{-1} correspond to different vibration modes of V=O, with the peak at 765 cm^{-1} specifically corresponding to the V—O bond.[40] These results confirm the existence of NVO. The formation of the peak at 1171 cm^{-1} may be attributed to the formation of C—N bonds following the introduction of PANI.[41] Similarly, the peaks at 1503 cm^{-1} and 1587 cm^{-1} are assigned to the C=C and C–C stretching vibrations of aromatic rings, respectively. To gain deeper insights into the surface chemical composition and elemental valence states of the NVOP-3 composite, we systematically performed X-ray photoelectron spectroscopy (XPS) characterization. The full-spectrum analysis shown in Figure S5, Supporting Information confirms the presence of five characteristic elements (Na, O, V, C, and N) on the material surface. The distinct signals of N and C elements verify the successful formation of the PANI coating layer. Peak analysis of the high-resolution V 2p spectrum (Figure 2d) reveals that the V 2p orbital exhibits characteristic doublets of V^{5+} at binding energies of 517.0 eV and 524.6 eV, with additional characteristic signals of V^{4+} observed at 515.8 eV and 523.2 eV. The coexistence of the V^{4+}/V^{5+} mixed valence states is conducive to promoting the kinetics of Zn^{2+} insertion/extraction reaction through a valence interconversion mechanism. Figure 2e presents the N 1s spectrum of NVOP-3, where two fitted components at 399.6 and 401.7 eV are attributed to –N= and –NH– groups in PANI, respectively. This molecular configuration is favorable for constructing an electron conduction network. In the C 1s spectrum (Figure 2f), three characteristic peaks are observed at 284.8 eV (C–C/C=C), 286.2 eV (C–N), and 289.1 eV (C=N), further confirming the presence of benzene ring structures.[42,43] As shown in Figure S6, Supporting Information the O1s spectrum exhibits deconvoluted peaks at 529.8 eV, 531.7 eV, and 533.4 eV, which are assigned to the O—V bond, oxygen vacancies, and O—Na bond, respectively. The relative area content of O 1s spectral peaks of NVO and NVOP-3 is listed in Table S1, Supporting Information. Obviously, NVOP-3 exhibits a higher oxygen vacancy content than NVO, where the significant increase in oxygen vacancies is attributed to the in situ polymerization reaction during the preparation process. Specifically, when NVO oxidizes aniline monomers, lattice oxygen is detached from the interface to compensate for the consumption of oxidant, thereby generating oxygen vacancies.[43,44]

To assess the electrochemical performance of the as-prepared materials as cathodes in AZIBs, CR2032-type coin cells were assembled with zinc foil serving as the anode and a 2 M

Zn(CF$_3$SO$_3$)$_2$ aqueous solution as the electrolyte. The thickness of the PANI coating layer was regulated by varying the duration of aniline's self-initiated polymerization. The reversible capacity of NVOP samples (Figure S7, Supporting Information) prepared with different reaction times is higher than that of NVO, with the highest reversible capacity achieved at a reaction time of 1.5 h. Additionally, in the long-cycle test, the battery exhibited the highest capacity retention when the reaction time was 1.5 h. Based on its excellent electrochemical performance, this reaction time was determined as optimal and used for subsequent testing and characterization.

Figure 3a demonstrates the electrochemical performance of the fabricated Zn//NVOP-3 cell, showing cyclic voltammetry (CV) curves at 0.2 mV s^{-1} between 0.4 and 1.6 V (vs Zn^{2+}/Zn). Two distinct redox pairs are observed at 0.933/0.783 V and 0.648/0.464 V, which are attributed to the multistep insertion and extraction of Zn^{2+} and H$^+$ ions. The response current of each redox peak of NVOP-3 material is higher than that of NVO, demonstrating that the effective coating of PANI enhances the electron transport of the material, which can reduce the polarization of the electrochemical reaction in the charge/discharge process.[20,45] The CV curve of NVOP-3 at 0.2 mV s^{-1} (Figure 3b) almost overlaps after the first cycle, manifesting that the electrochemical zinc storage behavior of NVOP-3 in 2 M Zn(CF$_3$SO$_3$)$_2$ is highly reversible. As displayed in Figure 3c, the galvanostatic charge/discharge (GCD) profiles of NVO and NVOP-3 at 0.1 A g^{-1} are tested. Obviously, the voltage gaps of the voltage platform during charge/discharge are smaller for NVOP-3 than for NVO, demonstrating that the PANI coating is beneficial for reducing the polarization of the NVO cathode. Subsequently, the rate capability of the samples was evaluated and demonstrated in Figure 3e. The discharge specific capacities of NVOP-3 are 301.5, 278.1, 249.6, 220.4, 185.3, and 129.3 mAh g^{-1} at current densities of 0.1, 0.2, 0.5, 1, 2, and 5 A g^{-1}, respectively, which are significantly higher than those of NVO. Owing to the excellent conductivity of the PANI coating layer, NVOP-3 can deliver a higher specific capacity than NVO at high currents. Moreover, when the current is restored to 0.1 A g^{-1}, NVOP-3 can quickly recover to its initial high reversible capacity without obvious attenuation. Additionally, the NVOP-3 electrode can maintain the shape of its GCD curves at various current densities, further demonstrating the remarkable rate capability of NVOP-3 (Figure 3d). The electrochemical cycling stability of Zn//NVOP-3 cell is depicted in Figure 3f. The capacity retention rate of NVOP-3 at 2 A g^{-1} is as high as 92.5% after 1000 cycles, while that of NVO is only 73.7% under the same conditions. To demonstrate the practical application of the NVOP-3 material, we have assembled a 65 mAh soft-pack battery and evaluated its electrochemical performance. As shown in Figure S8, Supporting Information after 100 cycles at a current density of 0.5 A g^{-1}, a capacity retention of 87.9% can still be maintained. In addition, the assembled Zn//NVOP-3 soft-pack batteries connected in series can power a thermohydrometer for several days, further confirming their practical applicability. As presented in Figure S9, Supporting Information the NVOP-3 electrode retains a well-preserved nanobelt morphology after 200 cycles, whereas the bare NVO counterpart exhibits
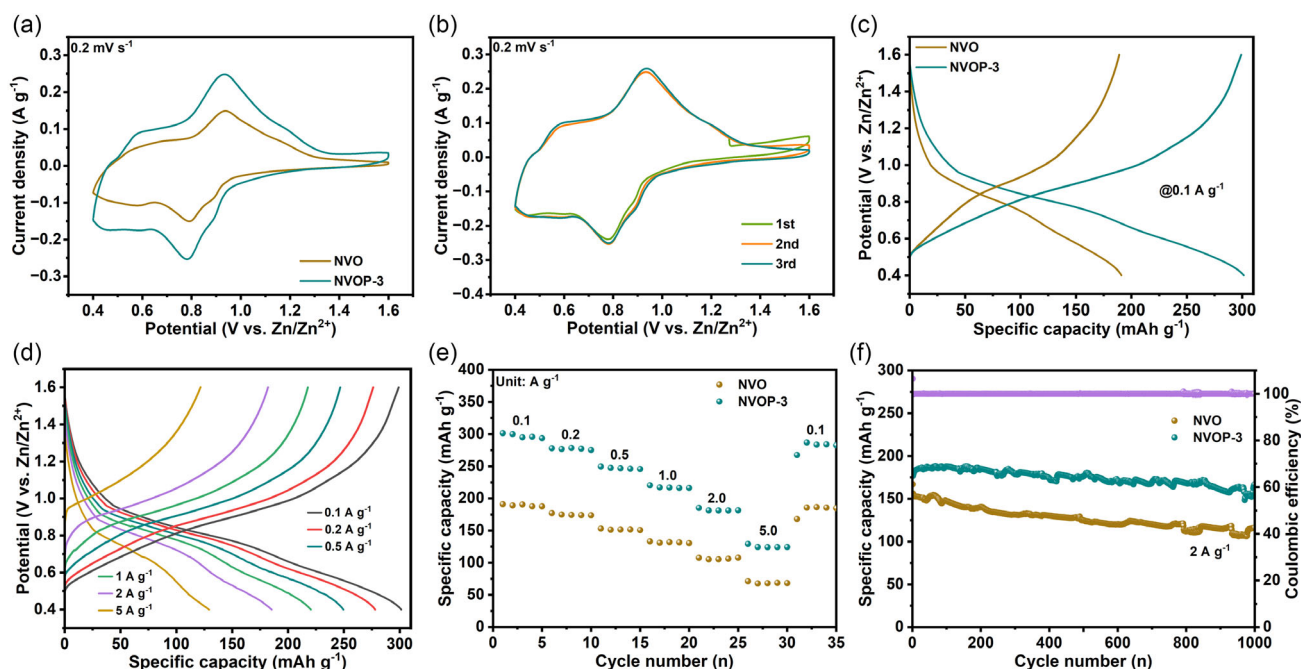
Batteries & Supercaps

Research Article
doi.org/10.1002/batt.202500583

Chemistry Europe
European Chemical
Societies Publishing

Figure 3. Electrochemical performance of NVO and NVOP-3 electrodes. a) CV curves tested at 0.2 mV s^{-1}. b) CV curves of the NVOP-3 cathode at 0.2 mV s^{-1}. c) GCD curves at 0.1 A g^{-1}. d) GCD profiles of the NVOP-3 cathode at different currents. e) Rate capability of the NVO and NVOP-3 cathode. f) Cycling performance at 2 A g^{-1}.

severe nanobelt fracture and structural disintegration under identical cycling conditions (Figure S10, Supporting Information). To further confirm that the PANI can improve the structural integrity of NVO, the NVO and NVOP-3 were immersed in a 2 M Zn(CF$_3$SO$_3$)$_2$ electrolyte for 5 days. Obviously, the NVO was found to dissolve into the electrolyte, and the color of the electrolyte turned yellow due to NVO dissolution, while NVOP-3 showed no significant dissolution (Figure S11, Supporting Information). These results clearly indicate that the PANI coating not only enhances the conductivity of NVO but also alleviates the structural damage of NVO caused by ion insertion during cycling and prevents its dissolution. To investigate the reversible stability of the NVOP-3 cathode during charge/discharge processes, ex situ XPS measurements were performed (Figure S12, Supporting Information). Compared to the pristine state, discharging NVOP-3 to 0.4 V resulted in a significant decrease in the V^{5+} proportion and the emergence of characteristic V^{3+} peaks, which are directly attributed to the vanadium reduction reaction induced by Zn^{2+} insertion. Upon charging to 1.6 V, the V^{5+} proportion recovered, the V^{4+} proportion decreased, and the V^{3+} peaks vanished, which clearly demonstrates the oxidation of vanadium accompanying Zn^{2+} extraction. Critically, when the cathode was discharged again to 0.4 V, the V^{3+} peaks reappeared. Similarly, when discharged to 0.4 V, the distinct characteristic peak of Zn emerges owing to the insertion of Zn^{2+}. Upon further charging to 1.6 V, this Zn peak weakens as a result of the deintercalation of Zn^{2+}. These highly reversible valence changes between V^{5+} and V^{3+} throughout the charge/discharge cycle provide compelling evidence for the highly reversible redox reactions occurring in NVOP-3 during Zn^{2+} insertion/extraction. To investigate the effect of H$^+$ on the storage behavior of NVOP-3, Zn(CF$_3$SO$_3$)$_2$/acetonitrile (ACN) electrolyte

was prepared according to previous works.[46–48] As shown in Figure S13, Supporting Information the NVOP-3 electrode delivered a capacity of 140.8 mAh g^{-1} in 0.5 M Zn(CF$_3$SO$_3$)$_2$/ACN electrolyte, indicating that the charge storage process in NVOP-3 is primarily contributed by both Zn$^+$ and H$^+$, and the capacity contribution from H$^+$ can be calculated to be 53.3%. Notably, NVOP-3 demonstrates remarkable electrochemical performance not only in high-conductivity Zn(CF$_3$SO$_3$)$_2$ aqueous electrolytes but also in economically favorable ZnSO$_4$ aqueous solutions (Figure S14, Supporting Information). In particular, the 70.2% capacity retention after 1000 cycles in ZnSO$_4$ confirms that the PANI coating effectively suppresses vanadium dissolution even in this low-cost medium, thereby avoiding the performance degradation typically associated with sulfate-based electrolytes in vanadium oxides.[49]

To further investigate the reaction kinetics of the as-prepared NVO and NVOP-3 samples, CV profiles at varying scan rates were determined in **Figure 4**a and Figure S15, Supporting Information. Notably, the CV profiles retain their shape with increasing scan rate while exhibiting progressively larger areas. Concurrently, cathodic peaks shift toward lower potentials and anodic peaks toward higher potentials, demonstrating excellent reversibility. The peak current (*i*) and scan rate (*v*) relationship follows the power-law (Equation (1)):[50]

$$i = av^b \tag{1}$$

$$\log i = \log a + b \log v \tag{2}$$

Here, *a* and *b* are fitting parameters, and the *b*-value, obtained by linearizing (Equation 2), determines the charge storage

Batteries & Supercaps

Research Article
doi.org/10.1002/batt.202500583

Chemistry
Europe
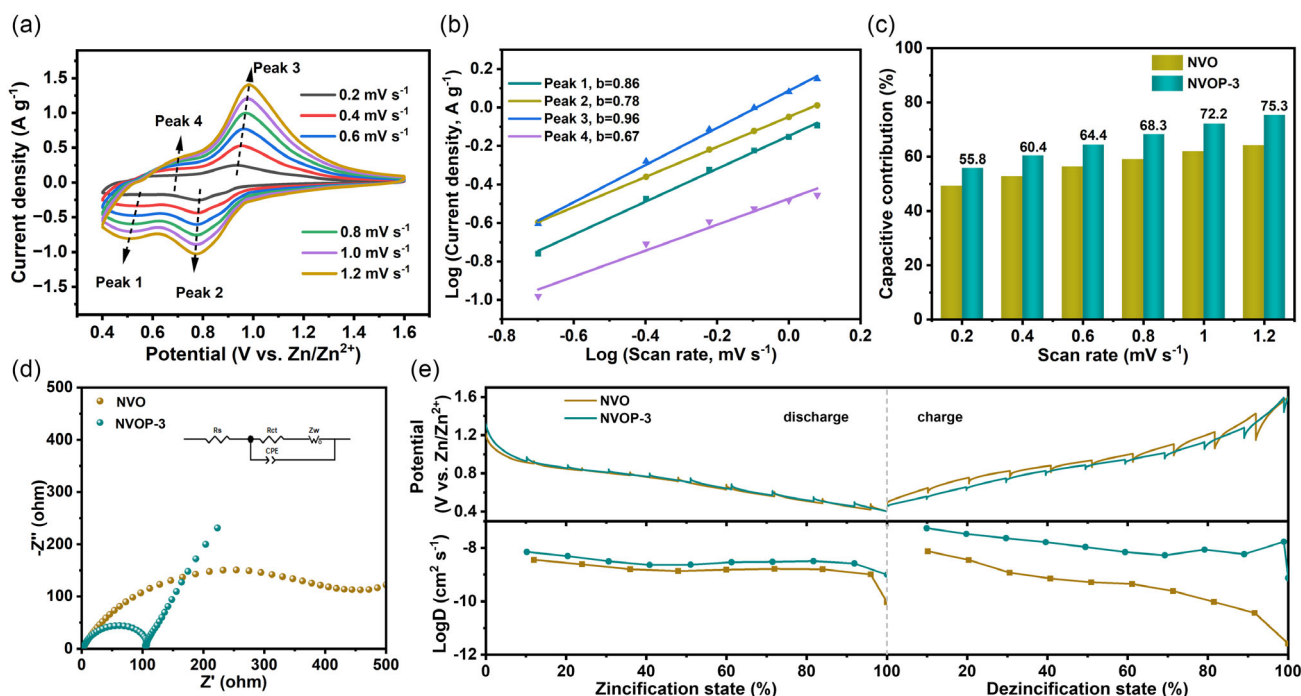
European Chemical
Societies Publishing

Figure 4. Kinetic assessment performed for NVOP-3. a) CV curves of the NVOP-3 cathode. b) Plot of log(i) versus log(v). c) Contribution ratios of capacitance at different scan rates in NVO and NVOP-3. d) EIS of NVO and NVOP-3 electrodes. e) GITT profiles and corresponding ion diffusion coefficient of NVO and NVOP-3.

kinetics: a b-value approaching 0.5 suggests diffusion-controlled behavior, whereas a b-value near 1 indicates capacitive-dominated processes. As depicted in Figure 4b, the calculated b values for the four peaks are 0.86, 0.78, 0.96, and 0.67, respectively. These values demonstrate mixed diffusion and capacitive control of the electrochemical reaction.

To further quantify the contribution of pseudocapacitive behavior to the overall electrochemical process, (Equation (3)) is employed. This equation decomposes the total current response (i) into two components, where k_1v represents the current contribution from capacitive behavior, and $k_2v^{1/2}$ corresponds to the current arising from diffusion behavior.[51]

$$i(v) = k_1 v + k_2 v^{1/2} \tag{3}$$

$$\frac{i(v)}{v^{\frac{1}{2}}} = k_1 v^{1/2} + k_2 \tag{4}$$

The (Equation (4)) is derived through deformation. This linear equation can be used to calculate k_1, and the ratio of the Faradaic capacitive contribution to the total capacitive contribution can be subsequently obtained. As shown in Figure 4c and Figure S16, Supporting Information the capacitive contribution ratios of both NVO and NVOP-3 increase gradually as the scan rate rises from 0.2 to 1.2 mV s^{-1}. Compared with NVO, NVOP-3 exhibited a significantly higher capacitive contribution at all tested scan rates, reaching 75.3% at 1.2 mV s^{-1}. This finding aligns with the calculated b-values and further confirms that the PANI coating can effectively enhance the rapid transport of ions and electrons during charge/discharge processes. This underscores the critical role

of PANI in optimizing the electrochemical kinetics of the NVOP-3 cathode.

Figure 4d displays the electrochemical impedance spectroscopy (EIS) spectra of NVO and NVOP-3. The high-frequency semicircle represents charge transfer resistance (R_{ct}), while the low-frequency linear region is associated with the diffusion resistance (R_s). Equivalent circuit fitting reveals that NVOP-3 exhibits an extremely low R_{ct} value of 102.2 Ω, which is significantly lower than that of NVO (418.9 Ω). This result confirms that NVOP-3 has accelerated charge transfer kinetics and enhanced electrical conductivity, ensuring rapid ion insertion/extraction during charge/discharge cycles and thus significantly improving the electrochemical performance of the electrode material. The drastic reduction in R_{ct} further underscores the critical role of the PANI coating in optimizing interfacial charge transfer and ion diffusion. As shown in Figure S17 and Table S2, Supporting Information EIS experiments at different cycling stages (i.e., the first, 20th, and 50th cycles) were also conducted. Obviously, the values of R_s are almost unchanged, manifesting that the electrode structure is stable during the cycles. For the R_{ct}, the values are relatively small, with only a slight increase observed after 50 cycles. This demonstrates excellent ion transport performance and stable charge transfer behavior at the electrode–electrolyte interface. Figure 4e presents the galvanostatic intermittent titration technique (GITT) profiles of NVOP-3 and NVO. As anticipated, the calculated ionic diffusion coefficient of NVOP-3 ranges from 10^{-9} to 10^{-8} cm^2 s^{-1}, approximately one order of magnitude higher than that of NVO (10^{-10} to 10^{-9} cm^2 s^{-1}). This significant enhancement in ionic diffusivity aligns with the EIS results, further

demonstrating that the PANI coating effectively improves ion transport kinetics and structural integrity, thereby contributing to the superior electrochemical performance of NVOP-3.

3. Conclusion

In conclusion, a PANI-coated NVO composite was successfully prepared via a hydrothermal and in situ polymerization approach to enhance the Zn^{2+} storage capacity and structural integrity of NVO. The core–shell structured NVOP-3 exhibits a high specific capacity of 301.5 mAh g^{-1} at 0.1 A g^{-1}, retains a capacity of 129.3 mAh g^{-1} at 5 A g^{-1}, and achieves a high capacity retention of 92.5% after 1000 cycles at 2 A g^{-1}. These performance enhancements are ascribed to the synergistic effects of the PANI coating, which effectively improves ion/electron migration and structural integrity. This study offers new perspectives on the design of high-stability vanadium-based cathodes for AZIBs, highlighting the critical role of conductive polymer coatings in optimizing interfacial kinetics and structural robustness.

Conflict of Interest

The authors declare no conflict of interest.

Data Availability Statement

The data that support the findings of this study are available from the corresponding author upon reasonable request.

[1] Z. Yang, J. Zhang, M. C. W. Kintner-Meyer, X. Lu, D. Choi, J. P. Lemmon, J. Liu, *Chem. Rev.* **2011**, *111*, 3577.
[2] B. Dunn, H. Kamath, J.-M. Tarascon, *Science* **2011**, *334*, 928.
[3] M. Armand, J.-M. Tarascon, *Nature* **2008**, *451*, 652.
[4] F. Zhao, B. Wang, B. Huang, W. Zhang, J. Chen, L. Liu, H. Wang, A. Y. Elezzabi, P. S. Lee, D. J. Milliron, W. W. Yu, H. Li, *Nat. Rev. Clean Technol.* **2025**, *1*, 396.
[5] J. Yu, L. Gao, G. Qiao, S. Wang, Y. Tang, Z. Deng, C. Wei, Y. Hou, S. Li, *Compos. B Eng.* **2026**, *309*, 113055.
[6] M. Li, J. Lu, Z. Chen, K. Amine, *Adv. Mater.* **2018**, *30*, 1800561.
[7] J.-Y. Hwang, S.-T. Myung, Y.-K. Sun, *Chem. Soc. Rev.* **2017**, *46*, 3529.
[8] K.-Y. Zhang, Z.-Y. Gu, E. H. Ang, J.-Z. Guo, X.-T. Wang, Y. Wang, X.-L. Wu, *Mater. Today* **2022**, *54*, 189.
[9] L. Gao, M. Cao, C. Zhang, J. Li, X. Zhu, X. Guo, Z. Toktarbay, *Adv. Compos. Hybrid Mater.* **2024**, *7*, 144.
[10] L. Shi, R. Jiao, D. Lan, L. Wang, Y. Gao, M.-F. Lin, Z. Lang, W. He, G. Jia, J. Cui, S. Li, *Chem. Eng. J.* **2025**, *519*, 165074.
[11] Y. Chen, S. Li, J. Chen, L. Gao, P. Guo, C. Wei, J. Fu, Q. Xu, *J. Colloid Interface Sci.* **2024**, *664*, 726..
[12] D. Chao, W. Zhou, F. Xie, C. Ye, H. Li, M. Jaroniec, S.-Z. Qiao, *Sci. Adv.* **2020**, *6*, eaba4098.
[13] Z. Liu, Y. Huang, Y. Huang, Q. Yang, X. Li, Z. Huang, C. Zhi, *Chem. Soc. Rev.* **2020**, *49*, 180.
[14] G. Fang, J. Zhou, A. Pan, S. Liang, *ACS Energy Lett.* **2018**, *3*, 2480.
[15] J. Song, K. Xu, N. Liu, D. Reed, X. Li, *Mater. Today* **2021**, *45*, 191.
[16] L. Gao, Y. Ma, C. Zhang, M. Cao, *J. Alloys Compd.* **2023**, *968*, 172008.
[17] L. Zhang, Y. Chen, Z. Jiang, J. Chen, C. Wei, W. Wu, S. Li, Q. Xu, *Energy Environ. Mater.* **2024**, *7*, e12507.
[18] T. Wang, S. Li, X. Weng, L. Gao, Y. Yan, N. Zhang, X. Qu, L. Jiao, Y. Liu, *Adv. Energy Mater.* **2023**, *13*, 2204358.
[19] X. Ma, X. Cao, M. Yao, L. Shan, X. Shi, G. Fang, A. Pan, B. Lu, J. Zhou, S. Liang, *Adv. Mater.* **2022**, *34*, 2105452.
[20] M. Yan, P. He, Y. Chen, S. Wang, Q. Wei, K. Zhao, X. Xu, Q. An, Y. Shuang, Y. Shao, K. T. Mueller, L. Mai, J. Liu, J. Yang, *Adv. Mater.* **2018**, *30*, 1703725.
[21] Y. Liu, C. Lu, Y. Yang, W. Chen, F. Ye, H. Dong, Y. Wu, R. Ma, L. Hu, *Adv. Mater.* **2024**, *36*, 2312982.
[22] L. E. Blanc, D. Kundu, L. F. Nazar, *Joule* **2020**, *4*, 771.
[23] B. Tang, L. Shan, S. Liang, J. Zhou, *Energy Environ. Sci.* **2019**, *12*, 3288.
[24] T. Wei, Q. Li, G. Yang, C. Wang, *J. Mater. Chem. A* **2018**, *6*, 8006.
[25] X. Yao, Y. Zhao, F. A. Castro, L. Mai, *ACS Energy Lett.* **2019**, *4*, 771.
[26] Z. Hao, J. Wang, J. Feng, Y. Fan, J. Peng, J. Wang, S. Dou, *Carbon Energy* **2025**, *7*, e681.
[27] M. Tian, C. Liu, J. Zheng, X. Jia, E. P. Jahrman, G. T. Seidler, D. Long, M. Atif, M. Alsalhi, G. Cao, *Energy Storage Mater.* **2020**, *29*, 9.
[28] P. Hu, T. Zhu, X. Wang, X. Wei, M. Yan, J. Li, W. Luo, W. Yang, W. Zhang, L. Zhou, Z. Zhou, L. Mai, *Nano Lett.* **2018**, *18*, 1758.
[29] C. Xiong, X. Lian, X. Yu, L. Zhong, N. Chen, G. Du, *J. Power Sources* **2025**, *641*, 236835.
[30] P. He, G. Zhang, X. Liao, M. Yan, X. Xu, Q. An, J. Liu, L. Mai, *Adv. Energy Mater.* **2018**, *8*, 1702463.
[31] J. Sun, Y. Zhao, Y. Liu, H. Jiang, D. Chen, L. Xu, T. Hu, C. Meng, Y. Zhang, *J. Colloid Interface Sci.* **2023**, *633*, 923.
[32] F. Zeng, Y. Xiao, Y. Shen, X. Xu, Z. Qin, *Electrochim. Acta* **2021**, *386*, 138516.
[33] Q. Pang, C. Sun, Y. Yu, K. Zhao, Z. Zhang, P. M. Voyles, G. Chen, Y. Wei, X. Wang, *Adv. Energy Mater.* **2018**, *8*, 1800144.
[34] K. Yu, X. Pan, G. Zhang, X. Liao, X. Zhou, M. Yan, L. Xu, L. Mai, *Adv. Energy Mater.* **2018**, *8*, 1802369.
[35] C. Liu, Z. Neale, J. Zheng, X. Jia, J. Huang, M. Yan, M. Tian, M. Wang, J. Yang, G. Cao, *Energy Environ. Sci.* **2019**, *12*, 2273.
[36] S. Boukhalfa, K. Evanoff, G. Yushin, *Energy Environ. Sci.* **2012**, *5*, 6872.
[37] M. Wang, J. Zhang, L. Zhang, J. Li, W. Wang, Z. Yang, L. Zhang, Y. Wang, J. Chen, Y. Huang, D. Mitlin, X. Li, *ACS Appl. Mater. Interfaces* **2020**, *12*, 31564.
[38] Y. Liu, Z. Pan, D. Tian, T. Hu, H. Jiang, J. Yang, J. Sun, J. Zheng, C. Meng, Y. Zhang, *Chem. Eng. J.* **2020**, *399*, 125842.
[39] M. Huang, Y. Mai, L. Zhao, X. Liang, Z. Fang, X. Jie, *Electrochim. Acta* **2021**, *388*, 138624.
[40] T. Wei, Q. Li, G. Yang, C. Wang, *J. Mater. Chem. A* **2018**, *6*, 20402.
[41] J. Tokarský, L. Maixner, P. Peikertová, L. Kulhánková, J. V. Burda, *Eur. Polym. J.* **2014**, *57*, 47.
[42] A. B. Olabintan, T. A. Saleh, A. Al-Ahmed, *J. Energy Storage* **2025**, *120*, 116426.
[43] X.-W. Liang, Y.-Y. Yang, W.-F. Di, S.-Y. Chen, R. Zhang, J. Hu, D. Lin, Y. Huo, *Chem. Eng. J.* **2024**, *495*, 153255.
[44] W.-F. Di, Q. Zhang, R.-H. Wang, X.-W. Liang, R. Zhang, Q. Zheng, J. Liu, D. Lin, Y. Huo, *Small* **2025**, *21*, e06528.
[45] X. Guo, G. Fang, W. Zhang, J. Zhou, L. Shan, L. Wang, C. Wang, T. Lin, Y. Tang, S. Liang, *Adv. Energy Mater.* **2018**, *8*, 1801819.
[46] R. Zhang, D. Luo, H. Xu, J. Wang, H. Dou, X. Zhang, *Chem. Eng. J.* **2023**, *476*, 146741.
[47] R. Zhang, H. Xu, Z. Li, H. Dou, X. Zhang, *Adv. Funct. Mater.* **2025**, *35*, 2424649.

Batteries & Supercaps

Research Article
doi.org/10.1002/batt.202500583

Chemistry Europe
European Chemical
Societies Publishing

[48] W. Wang, V. S. Kale, Z. Cao, Y. Lei, S. Kandambeth, G. Zou, Y. Zhu, E. Abouhamad, O. Shekhah, L. Cavallo, M. Eddaoudi, H. N. Alshareef, *Adv. Mater.* **2021**, *33*, 2103617.

[49] H. Zhao, M. Wan, X. Zhu, X. Cui, X. Du, R. Zheng, H. Zhong, H. Wang, *ACS Appl. Nano Mater.* **2024**, *7*, 23712.

[50] V. Augustyn, J. Come, M. A. Lowe, J. W. Kim, P.-L. Taberna, S. H. Tolbert, H. D. Abruña, P. Simon, B. Dunn, *Nat. Mater.* **2013**, *12*, 518.

[51] X. Wang, B. Xi, X. Ma, Z. Feng, Y. Jia, J. Feng, Y. Qian, S. Xiong, *Nano Lett.* **2020**, *20*, 2899.